Annual, Interannual, and Intraseasonal Variability of Tropical Tropopause Transition Layer Cirrus

KATRINA S. VIRTS AND JOHN M. WALLACE

Department of Atmospheric Sciences, University of Washington, Seattle, Washington

(Manuscript received 15 December 2009, in final form 16 April 2010)

ABSTRACT

Cloud fields based on the first three years of data from the Cloud–Aerosol Lidar and Infrared Pathfinder Satellite Observations (CALIPSO) mission are used to investigate the relationship between cirrus within the tropical tropopause transition layer (TTL) and the Madden–Julian oscillation (MJO), the annual cycle, and El Niño–Southern Oscillation (ENSO).

The TTL cirrus signature observed in association with the MJO resembles convectively induced, mixed Kelvin–Rossby wave solutions above the Pacific warm pool region. This signature is centered to the east of the peak convection and propagates eastward more rapidly than the convection; it exhibits a pronounced eastward tilt with height, suggestive of downward phase propagation and upward energy dispersion. A cirrus maximum is observed over equatorial Africa and South America when the enhanced MJO-related convection enters the western Pacific. Tropical-mean TTL cirrus is modulated by the MJO, with more than twice as much TTL cirrus fractional coverage equatorward of 10° latitude when the enhanced convection enters the Pacific than a few weeks earlier, when the convection is over the Indian Ocean.

The annual cycle in cirrus clouds around the base of the TTL is equatorially asymmetric, with more cirrus observed in the summer hemisphere. Higher in the TTL, the annual cycle in cirrus clouds is more equatorially symmetric, with a maximum in the boreal winter throughout most of the tropics. The ENSO signature in TTL cirrus is marked by a zonal shift of the peak cloudiness toward the central Pacific during El Niño and toward the Maritime Continent during La Niña.

1. Introduction

In the companion paper (Virts et al. 2010; hereafter, VWFA), we introduce an analysis protocol for relating features in the frequency of occurrence of cirrus clouds in the tropical tropopause transition layer (TTL), as observed by the polar-orbiting Cloud–Aerosol Lidar and Infrared Pathfinder Satellite Observations (CALIPSO), to fields of atmospheric variables throughout the tropics. The protocol involves the generation of a TTL cirrus index (cloud fraction; i.e., the fraction of the CALIPSO profiles acquired within a 10° latitude × 10° longitude box over a time interval of 7 days in which a cloud layer is observed with cloud base above 15 km or other specified levels). Figure 1 in that paper, reproduced here as Fig. 1, shows, in the top panel, a time series of 7-day running mean cloud fraction (as defined above) for a 10° latitude × 10° longitude region centered on Manus Island, Papua New Guinea (2°S, 147°E), together with a time series of cold point temperature derived from radiosonde observations at the observing station at Manus maintained by the U.S. Department of Energy's Atmospheric Radiation Measurement Program (ARM). High-pass filtered versions of both time series, generated with an 80-day Lanczos filter, are shown in the bottom panel of Fig. 1. The cloud fraction and cold point temperature time series are both marked by variability on three different time scales:

- **The annual cycle:** The tropical cold point tropopause exhibits a pronounced annual cycle: it is highest and coldest during the boreal winter (Reed and Vlcek 1969). The cycle was originally attributed to stronger and more deeply penetrating convection within the Hadley cell and was later linked to a ''stratospheric pump,'' driven by stratospheric planetary waves in extratropical latitudes. Stronger pumping during the boreal winter results in lower tropical cold point temperatures, allowing for deeper convection and

Corresponding author address: Katrina Virts, Department of Atmospheric Sciences, 408 ATG Bldg., Box 351640, Seattle, WA 98195–1640.
E-mail: kvirts@uw.edu

DOI: 10.1175/2010JAS3413.1

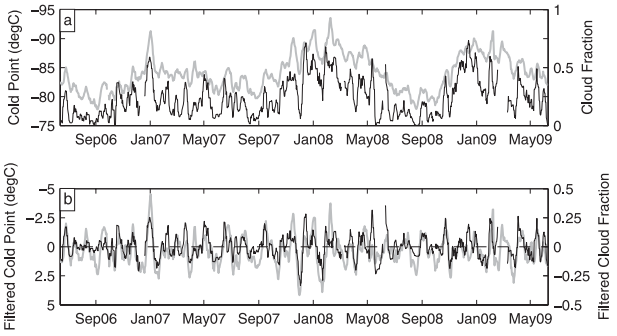

FIG. 1. (a) Seven-day running mean cold point temperature at Manus (gray; inverted scale at left) and CALIPSO cloud fraction with base above 15 km within a 10° latitude × 10° longitude region centered on Manus (black; scale at right) from June 2006 to June 2009. (b) As in (a), but an 80-day high-pass Lanczos filter has been applied to both variables. Originally Fig. 1 in VWFA.

a higher tropopause (Highwood and Hoskins 1998, and references therein). This cycle is clearly evident in the cold point temperature at the ARM site in Manus; the peak-to-peak amplitude is in the range of 6°–7°C. The lowest tropopause temperatures during each year were observed in January–February, and February 2008 was the coldest period, with 7-day running mean cold point temperatures dropping below −93°C. The highest cold point temperatures were observed during August–September of each year. Zhang (1993) found an annual cycle with similarly timed extrema in the fraction of high clouds (tops above 12.8 km) identified in outgoing longwave radiation (OLR) data from the tropics; he also reported that the annual cycle signal is stronger for clouds whose tops exceed 15 km. The annual cycle is evident in cloud fraction above Manus as well, with maximum TTL cirrus observed during the boreal winter, in agreement with previous observations of high cloud occurrence at Manus (Mather 2005). Seven-day running mean cloud fractions in Fig. 1 range from near zero during August/September to maxima in excess of 0.5 each January/February. The annual mean and annual cycle in TTL cirrus throughout the tropics are addressed in sections 2 and 3 of this paper, respectively.

- **Interannual variability:** Much of the interannual variability in Fig. 1 is related to El Niño–Southern Oscillation (ENSO). Dima and Wallace (2007) generated composites of tropical geopotential height and winds for the 10 strongest El Niño and La Niña months during the period 1979–2001 and found that the equatorial planetary wave signature at the 150-hPa level above the warm pool is strongly accentuated during the strongest La Niña episodes and only barely discernible during the strongest El Niño episodes. Yulaeva and Wallace (1994) found that Microwave Sounding Unit channel-4 (MSU-4; lower stratospheric) temperatures also tend to be lower during La Niña years. Some interannual variability in both cold point temperature and cloud fraction is apparent in the time series in Fig. 1a: of the three boreal winter seasons, the winter of 2007/08 was the coldest, with a mean December–February (DJF) cold point temperature of −88.8°C, and cloudiest, with a mean DJF cirrus fraction of 0.46, at Manus whereas the winter of 2006/07 was warmest (−84.9°C) and clearest (0.27). These differences are likely related to the pronounced La Niña event that was in progress during the former period. The impact of ENSO on TTL cirrus throughout the tropics is discussed in section 4.
- **Intraseasonal variability:** Variability in the tropical troposphere on intraseasonal time scales (roughly 20–60 days) is dominated by the Madden–Julian oscillation [MJO; alternately referred to as the tropical intraseasonal oscillation (ISO); Zhang 2005]. In previous studies, the MJO was recognized in surface pressure and OLR data as a region of disturbed weather that appears first over the Indian Ocean and propagates eastward along the equator into the western and central Pacific. Accompanying the convection are low-level convergent winds and a planetary-scale circulation in the zonal plane with strong upper tropospheric zonal wind anomalies (Madden and Julian 1971, 1972; Zhang 2005). Madden and Julian (1972) suggested that the convective centers might be accompanied by an eastward-propagating wave near the tropopause that circumnavigates the globe. Subsequent research has identified such a feature in the upper-level divergent component of the wind field (Knutson and Weickmann 1987), in Microwave Sounding Unit channel-2 mid- to upper tropospheric temperatures (Hendon and Salby 1994) and in upper tropospheric/TTL relative humidity data (Eguchi and Shiotani 2004). Hendon and Salby (1994) identified two classes of perturbations within the TTL in response to MJO convection: a coupled Rossby–Kelvin wave similar to that of Gill (1980) that migrates eastward along with the convective anomaly and a Kelvin wave that propagates eastward more rapidly than the convection and can be tracked as it propagates into the Western Hemisphere.

A relationship between TTL cirrus and the MJO has been demonstrated. In an analysis of five separate MJO episodes, Eguchi and Shiotani (2004) observed cirrus at the 100-hPa level to the east of the convective anomaly as it propagated into the western Pacific. They attributed the occurrence of the cirrus to the low temperatures produced by the convective system. Time series of 80-day high-pass filtered cold point

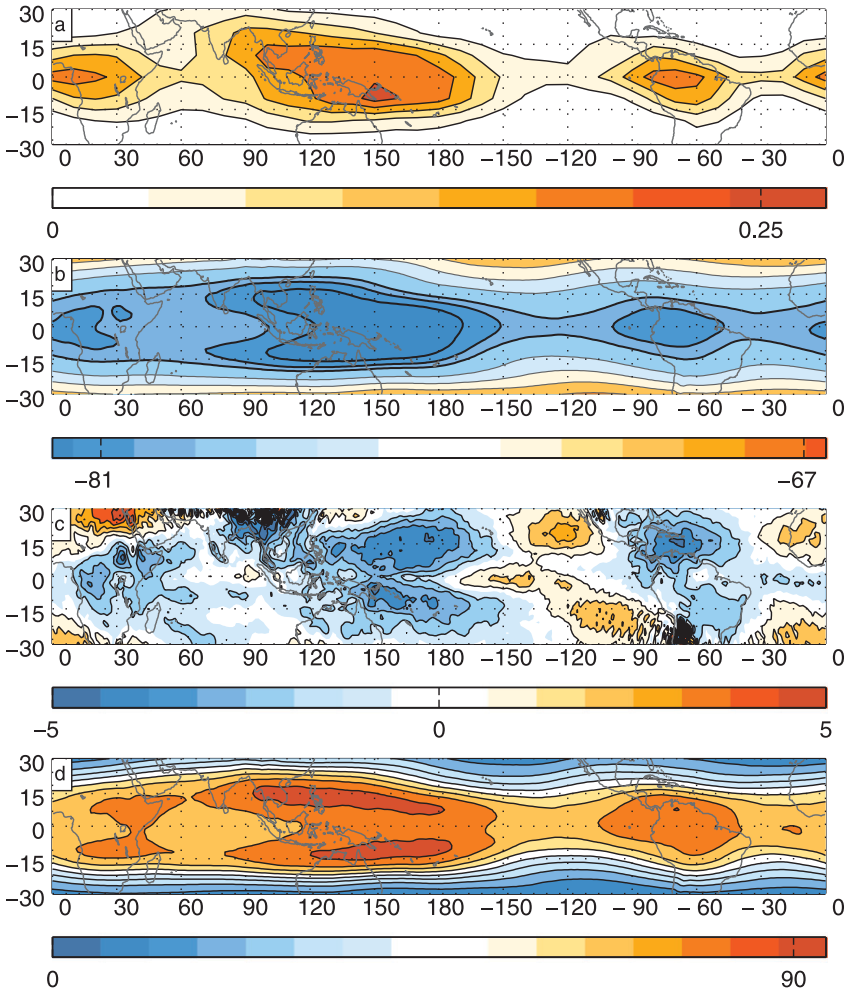

FIG. 2. Means for June 2006–June 2009 of (a) CALIPSO-derived cloud fraction with base above 15 km [contour interval (CI) = 0.05], (b) ERA 100-hPa temperature (contours at . . . −80, −79, −76, −73, . . . °C; outermost dark contour is −79°C), (c) ERA 100-hPa ω (CI = 0.001 Pa s^{-1}, with color bar including only lower magnitude velocities), and (d) ERA 100-hPa relative humidity (CI = 10%).

temperature and cloud fraction at Manus, shown in Fig. 1b, are highly correlated ($r \sim -0.61$). Furthermore, both raw and filtered time series of both variables exhibit a tendency for quasi-periodic behavior, with a 40-day rhythm, suggestive of an impact of the MJO on TTL temperature and cloud cover above Manus. The connection between the MJO and TTL cirrus throughout the tropics is explored in section 5.

In this paper, we will examine these relationships in further detail, considering both the spatial patterns of cloud fraction associated with these phenomena and the variations in cloud fraction over the tropics as a whole. For specifics on the datasets and analysis procedures used, including the definition of the CALIPSO-derived height-dependent cloud index, the reader is referred to section 2 of VWFA. When indicated, an 80-day high-pass Lanczos filter is applied to the time series of cloud fraction and environmental variables in order to eliminate the annual cycle and the interannual variability from the analysis.

2. Annual mean

Mean TTL cirrus fraction (calculated from CALIPSO data as cloud fraction with base above 15 km on a 10° latitude × 10° longitude grid, rather than on an overlapping 5° × 10° grid as in Fig. 3 of the companion paper) for the period June 2006–June 2009 is shown in the top panel of Fig. 2. In the annual mean, TTL cirrus clouds are identified most frequently—over 20% of the time—above a large region stretching from Southeast Asia

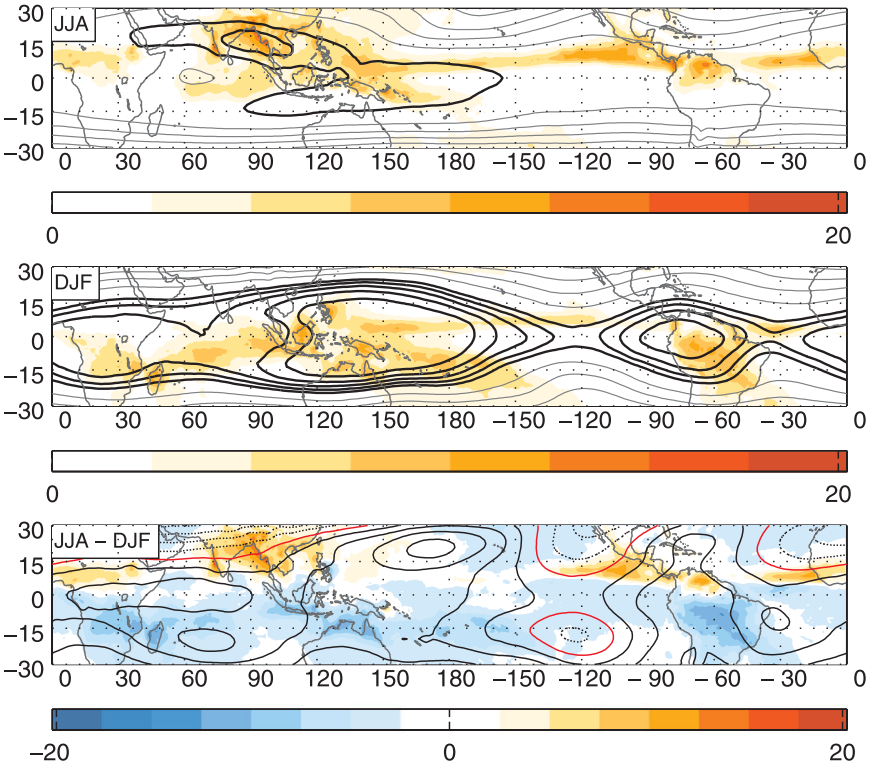

FIG. 3. Mean atmospheric conditions during (top) JJA and (middle) DJF, and (bottom) JJA − DJF. GPCP precipitation (mm day^{-1}) in colored shading, with CI = 3 mm day^{-1}. ERA-Interim 100-hPa temperature in contours, with contours at (top), (middle) . . . −80, −79, −76, −73, . . . °C (outermost dark contour is −79°C) and (bottom) every 2°C (zero contour is red).

southeastward across the Maritime Continent and into the western Pacific. More localized maxima are observed over equatorial Africa and South America. The Central Equatorial Pacific Experiment (CEPEX), conducted during March 1993, identified cirrus cloud decks with bases above 15 km in 29% of lidar return signals obtained during airborne investigations near the date line (McFarquhar et al. 2000). Other studies of subvisible tropical cirrus, such as Wang et al. (1996), have reported cloud frequencies as high as 70% over the western Pacific. Repeating the analysis of Fig. 2 for tropical cirrus with cloud bases above 12 km yields local values in the range of 0.5–0.6 (not shown). Characteristics of the annual mean cloudiness in the equatorial plane can be inferred from composites of the CALIPSO height-dependent cloud index that will be presented in section 4.

European Centre for Medium-Range Weather Forecasts (ECMWF) interim reanalysis (ERA-Interim) annual mean 100-hPa temperature, vertical velocity, and relative humidity are plotted in Figs. 2b–d, respectively. Comparing these with the cirrus climatology in Fig. 2a, it can be seen that TTL cirrus occurrence is negligible in regions of annual mean 100-hPa descent (e.g., above the subtropical eastern Pacific and northern Africa) but is also low in some regions of annual mean 100-hPa ascent (such as above the Caribbean Sea and southern China). A stronger correspondence is observed between regions of high TTL cirrus occurrence and low 100-hPa temperature and high relative humidity.

As noted in section 1, TTL cirrus occurrence varies on annual and interannual time scales. With just three years of data, a definitive analysis of these phenomena is not yet possible; however, the basic characteristics of this variability will be documented in the next two sections based on the three years of data available to date.

3. Annual cycle

The annual cycle in Global Precipitation Climatology Project (GPCP) precipitation and ERA-Interim 100-hPa temperature during the 3-yr CALIPSO period of record is shown in Fig. 3, in which mean values for the seasons June–August (JJA) and December–February are contrasted. The precipitation field during JJA is dominated by the Indian and Southeast Asian monsoon

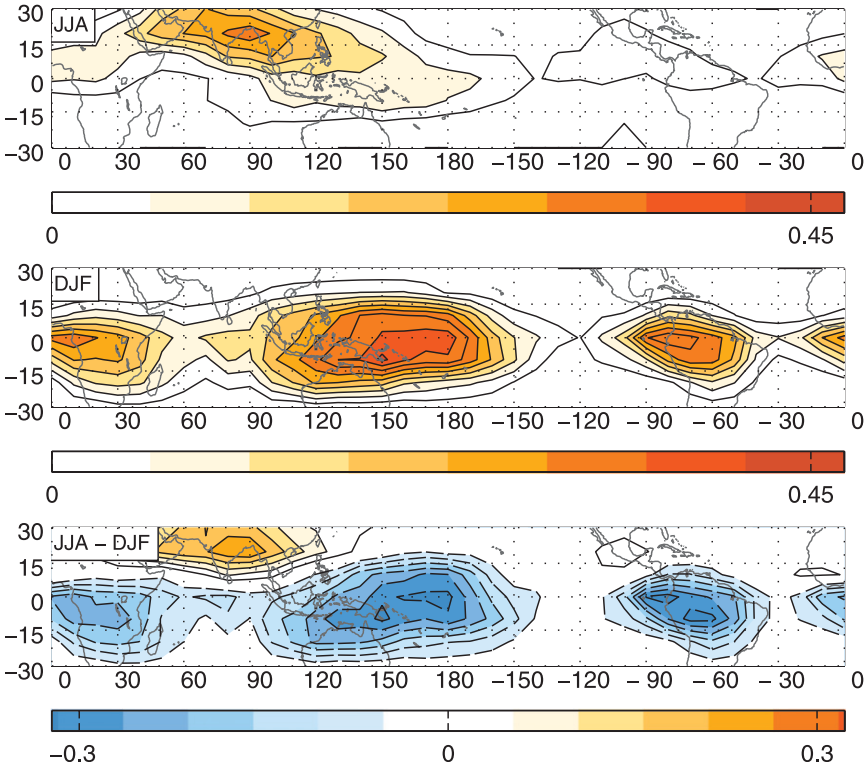

FIG. 4. As in Fig. 3, but for mean TTL cirrus fraction (base above 15 km, calculated on a 10° latitude × 10° longitude grid; CI = 0.05).

and by the Pacific and Atlantic intertropical convergence zones (ITCZs). The upper tropospheric anticyclone induced by the Indian monsoon is reflected in the temperature minimum centered over the Bay of Bengal. During DJF, there is a stationary, planetary wave signature above the warm pool reminiscent of the Gill (1980) convectively induced signature, and precipitation is heaviest over the South Pacific convergence zone (SPCZ), the Indian Ocean ITCZ, and tropical South America. The difference plot in the bottom panel is dominated by the contrast between the dry winter and wet summer hemispheres.

Analogous plots for the TTL cirrus index, a measure of the areal coverage of clouds with bases above 15 km, are shown in Fig. 4. The highest cloud fractions are observed during the months of December–February over the western equatorial Pacific, where an extensive region centered just south of the equator exhibits cloud fractions exceeding 0.4. During JJA, TTL cirrus occurrence is dominated by the Indian and Southeast Asian monsoon, in which cloud fractions in excess of 0.25 are observed from the Arabian Sea to the Indochina Peninsula (collocated with the temperature minimum in the top panel of Fig. 3). This Asian monsoon signature is also evident in plots of mean cloud fraction during each of the months June, July, and August (not shown). Massie et al. (2002) found similar patterns in boreal winter and summer tropical cirrus identified during the Halogen Occultation Experiment (HALOE). The difference plot in the bottom panel of Fig. 4 indicates that the Southern Hemisphere and equatorial belt both tend to be cloudier during DJF. Tropical-mean TTL cirrus fraction and 100-hPa temperature are plotted as 7-day running means equatorward of 10° latitude in Figs. 5a and 5b, respectively. Tropical-mean cloud fraction increases from 0.08 during JJA to 0.23 during DJF,

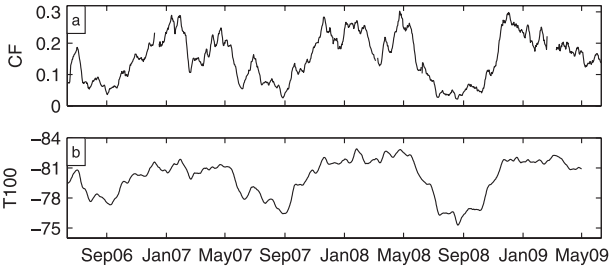

FIG. 5. (a) Seven-day running mean tropical-mean TTL cirrus fraction (cloud fraction with base above 15 km; equatorward of 10°). (b) As in (a), but for ERA 100-hPa temperature (scale is inverted).

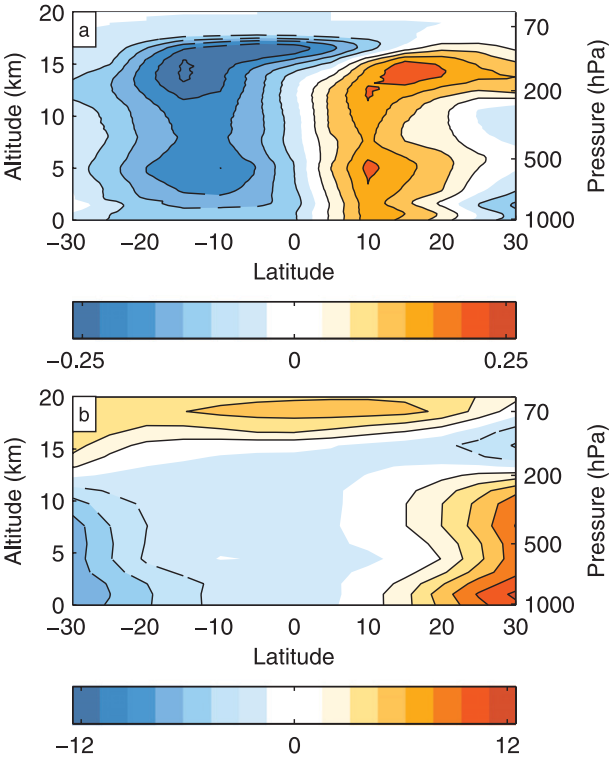

FIG. 6. Difference between July and January zonal-mean (a) cloud fraction (CI = 0.05) and (b) temperature (CI = 2°C). Positive values indicate cloudier/warmer July. Latitude resolution is 5°.

consistent with statistics compiled by Zhang (1993). In the mean over the entire tropics equatorward of 30° latitude, DJF TTL cirrus fraction is nearly twice as large as during JJA.

The different character of the annual cycle in the troposphere and in the TTL and lower stratosphere is documented in Fig. 6, which shows July minus January zonal-mean (top) cloud fraction and (bottom) temperature. At levels below ~14 km, the region of maximum cloud fraction and highest temperature shifts across the equator with the rising branch of the Hadley cell, whereas cloud fraction and temperature above ~16 km increase and decrease simultaneously throughout the tropics with the strengthening and weakening of the Brewer–Dobson circulation.

4. Interannual variability

A convenient measure of ENSO phase and intensity is the so-called ''cold tongue index'' (CTI), the departure of the sea surface temperature (SST) anomalies averaged over the region 6°S–6°N, 180°–90°W from the global-mean SST (Deser and Wallace 1990). CTI values during the period June 2006–June 2009 are plotted in Fig. 7. The CTI was weakly positive during the latter

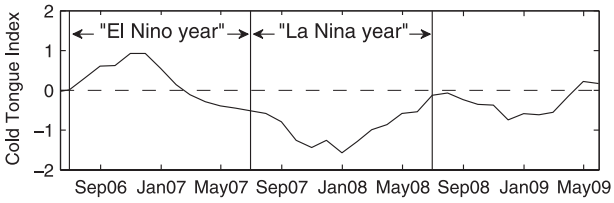

FIG. 7. Monthly values of CTI from June 2006 to June 2009. CTI is calculated by averaging SST anomalies within the region 6°S–6°N, 180°–90°W and subtracting from this the global mean SST. Anomalies are calculated relative to the period 1845–2008. Designated El Niño and La Niña years are indicated.

part of 2006 and early 2007. In March 2007, the CTI became negative, and pronounced La Niña conditions prevailed through most of the remainder of the record. In light of this behavior, we can represent the warm polarity of the ENSO cycle (i.e., El Niño) by the first year of the record and the cold polarity (La Niña) by the second year, as indicated by the vertical dividing lines in Fig. 7.

We begin by comparing the mean atmospheric fields during the El Niño and La Niña years. Figure 8 contrasts mean GPCP precipitation rates and 100-hPa temperatures for the two years. During the El Niño year, precipitation rates were higher over the western Pacific and along the Pacific ITCZ, and lower over the Maritime Continent and SPCZ, than during the La Niña year, in agreement with composites based on longer periods of record (Ropelewski and Halpert 1987). The convectively induced planetary wave signature over the Eastern Hemisphere was more pronounced during the La Niña year, in agreement with results of Dima and Wallace (2007). The difference plot (Fig. 8, bottom) reveals lobes of anomalously low temperatures flanking the equator near 150°W during the El Niño year; similar anticyclonic features in the geopotential height field were noted by Horel and Wallace (1981), Yulaeva and Wallace (1994), and Gettelman et al. (2001).

Mean TTL cirrus cloud fractions during the El Niño and La Niña years are contrasted in Fig. 9. During the El Niño year, TTL cirrus occurrence was highest over the western to central Pacific; this maximum shifted westward and strengthened during the La Niña year. As a result, more TTL cirrus was observed over the central Pacific, between 180° and 130°W, during the El Niño year, while cloud fractions over the Maritime Continent and western Pacific were as much as 40% larger during the La Niña year. A similar zonal shift in cirrus occurrence above the Maritime Continent and Pacific during the strong 1997–98 El Niño event was observed by Gettelman et al. (2001) based on boreal wintertime data from the HALOE experiment. Equatorial South America

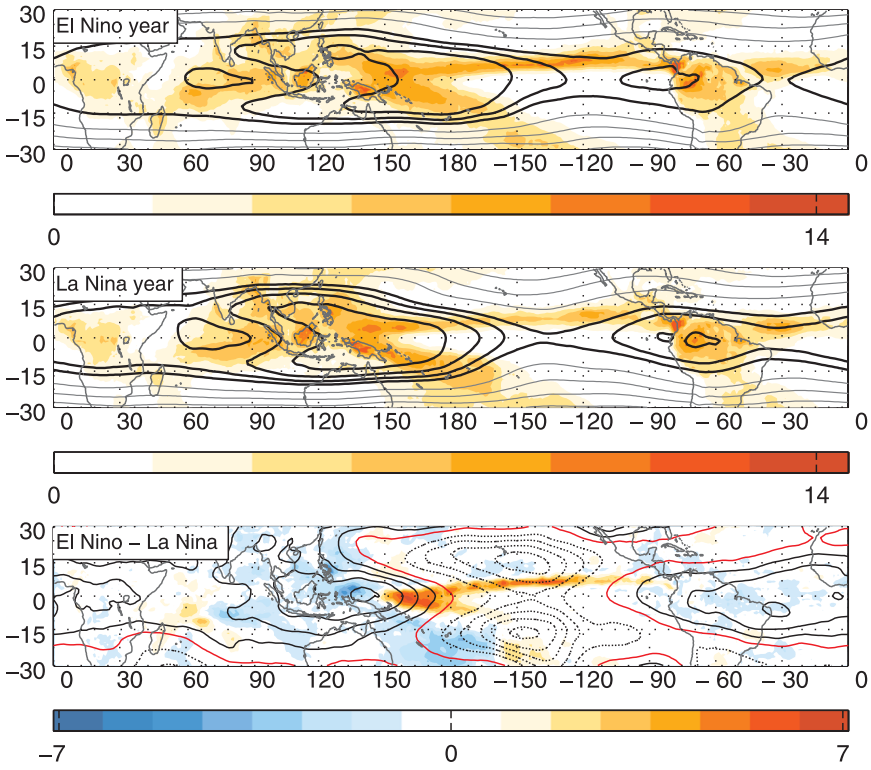

FIG. 8. As in Fig. 3, but mean conditions are plotted for (top) "El Niño year" (July 2006–June 2007) and (middle) "La Niña year" (July 2007–June 2008). Precipitation CI = (top), (middle) 1 mm day^{-1} and (bottom) 0.5 mm day^{-1}; temperature CI (bottom) = 2°C.

and, to a lesser degree, Africa also experienced more TTL cloudiness during the La Niña year.

Figure 10 shows analogous plots for the height-dependent cloud index, depicted as a vertical cross section in the equatorial plane. The primary convective regions above Africa, the Maritime Continent and western Pacific, and South America were evident during both the La Niña year and the El Niño year. While Fig. 10 shows a dry zone in the eastern Pacific, the convective clouds associated with the ITCZ in the central to eastern Pacific are more evident in a cross section centered to the north of the equator (not shown). During the El Niño year, a positive convective anomaly was centered just to the west of the date line, in association with the anomalously high precipitation in that region in Fig. 8. Convective activity above the Maritime Continent and South America was enhanced during the La Niña year, while the convective signature above Africa was quite similar during the two years. The strongest influence of ENSO on the cloud field was observed in the ~12–18-km layer, and the anomalous cirrus signature above the central Pacific during the El Niño year was centered near 13 km. Above the Maritime Continent, there was a clear tendency for increased cirrus cloud fraction during the La Niña year, particularly for cirrus within the TTL. The strongest ENSO cloud signal near South America was the enhanced TTL cirrus signature that was centered near 16-km altitude above the western coast of the continent during the La Niña year.

Examination of Figs. 9 and 10 reveals that the TTL was, on the whole, slightly cloudier during the La Niña year than the El Niño year. Tropical-mean (equatorward of 10°) TTL cirrus cloud fraction was 0.147 during the El Niño year versus 0.170 during the La Niña year (see Fig. 5).

5. Intraseasonal variability

a. Local characteristics

VWFA demonstrated that TTL cirrus is associated with planetary-scale waves over the Maritime Continent and western Pacific regions that resemble the theoretical solutions for the planetary wave response to an equatorial heat source. As noted in the discussion of Fig. 1, the filtered cold point temperature and cloud fraction time series at Manus exhibit cyclic behavior with a period of ~40 days. The Madden–Julian oscillation dominates variability in the 40–50-day range in the tropics and directly impacts the warm pool region (Madden and

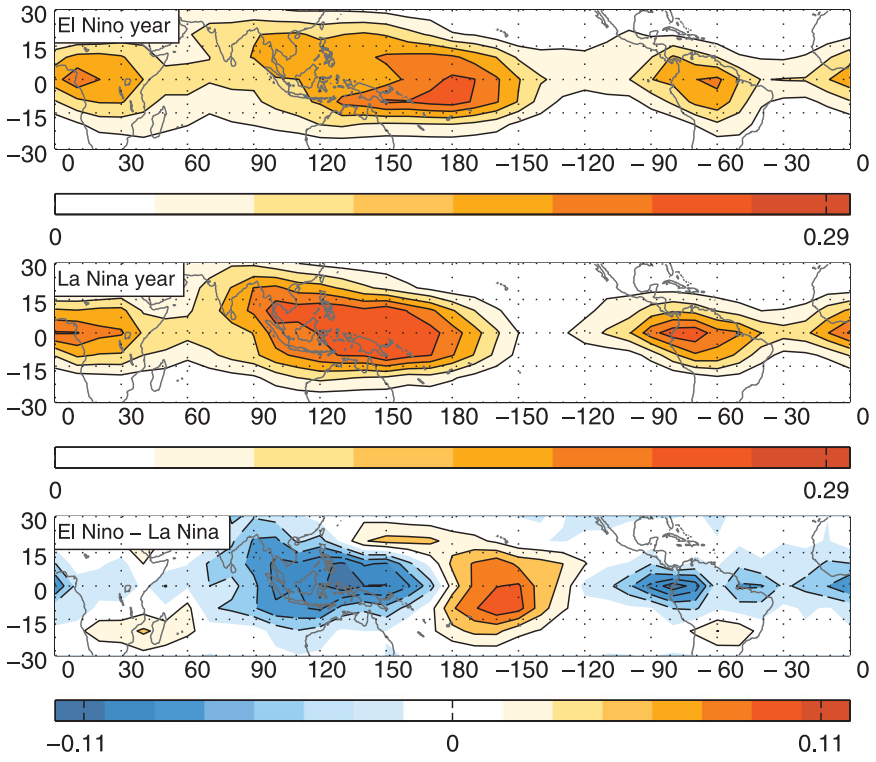

FIG. 9. As in Fig. 8, but for mean TTL cirrus fraction (base above 15 km). CI = (top), (middle) 0.05 and (bottom) 0.025.

Julian 1994; Zhang 2005). Thus, it seems reasonable to expect to observe an MJO signature in TTL cirrus.

To represent the time-varying state of the MJO, we will use the multivariate MJO index defined by Wheeler and Hendon (2004, hereafter WH). This index is a time series with two components that are calculated by projecting daily observations, with the annual cycle and components of the interannual variability removed, onto two empirical orthogonal functions (EOFs) of a multivariate field made up of near-equatorial OLR and lower- (850-hPa) and upper-tropospheric (200-hPa) zonal winds. The two components of the time-varying MJO index, Real-time Multivariate MJO series 1 (RMM1) and 2 (RMM2), are orthogonal and can be used to define the phase space illustrated in Fig. 11, which is a modified version of Fig. 7 in WH. The idealized evolution of the MJO, as represented on this chart, appears as a counterclockwise rotation. The geographic regions of enhanced MJO-related convection, as indicated in WH, are shown for reference. WH composited observations of wind, temperature, and other variables in terms of the eight sectors in this RMM1 versus RMM2 phase space. Here we linearly project the data onto the eight vectors indicated by the dashed lines in Fig. 11, each of which represents a different linear combination of the daily RMM1 and RMM2 indices. Before performing the projections, each of the MJO time series was adjusted to match the temporal resolution of the precipitation and TTL cirrus datasets and then renormalized.

The location and intensity of the convective activity associated with the MJO is shown in Fig. 12, in which filtered GPCP precipitation is regressed onto the time series for each phase of the MJO. Because of the way the phases have been defined, the regression patterns for phase 5 are of equal magnitude and opposite sign to those for phase 1, so patterns for only the first four phases are shown in Fig. 12. Phase 1 marks the onset of an MJO episode, with convection developing over the central equatorial Indian Ocean. The remnants of the previous active phase are visible along the date line near 10°S. In phase 2, these remnants have dissipated, while convection in the Indian Ocean has intensified and shifted eastward. The region of enhanced convection continues its eastward propagation through phase 4, weakening as it crosses the Maritime Continent because of interaction with local topography (Hsu and Lee 2005; Roundy 2008). In phase 5, the convective center emerges into the western Pacific, reintensifies, and begins to split in two, with one center focused on the ITCZ and the other on the SPCZ. In phases 7 and 8, only weak

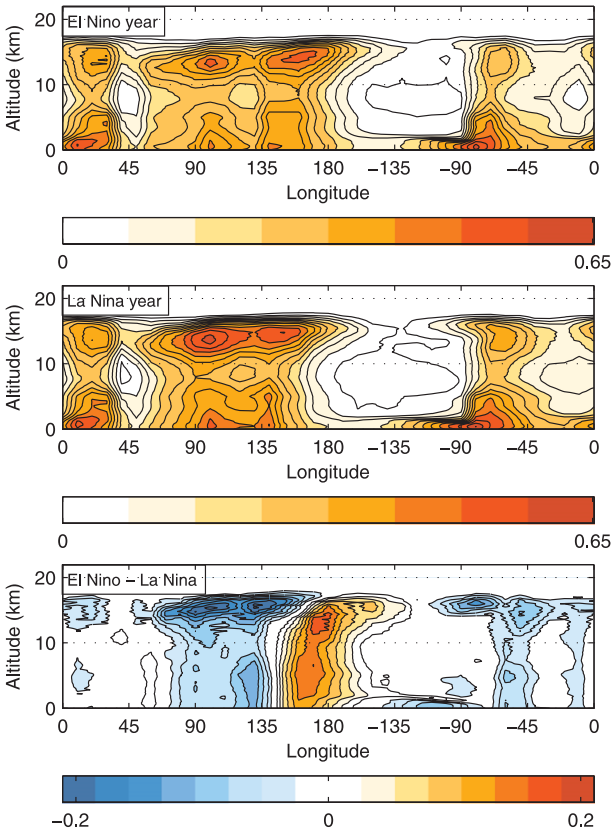

FIG. 10. As in Fig. 9, but for cloud fraction within 200-m layers from 5°S to 5°N.

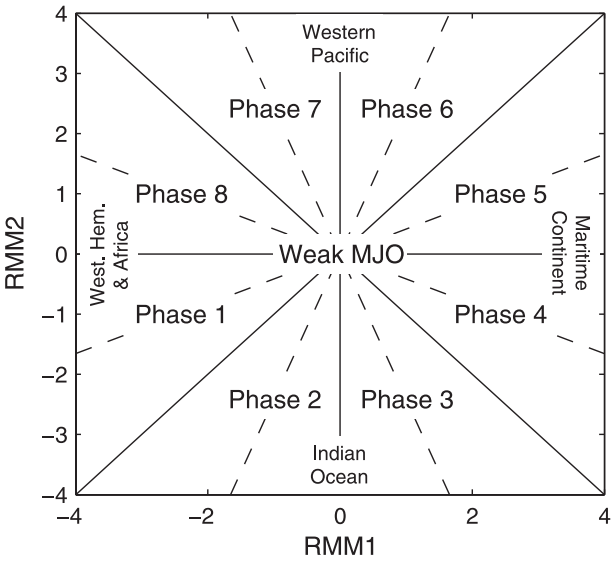

FIG. 11. Phase space defined by two components of MJO index created by Wheeler and Hendon (2004), with eight directional phase vectors. Modified from Fig. 7 of Wheeler and Hendon (2004), but retaining their indicated regions of maximum MJO-related convection.

remnants of the convective center are still evident in the Pacific. A weak precipitation signal is present near the Americas from phase 4 through 5; no connection with the African continent is observed. The existence and northward migration of precipitation anomalies over India (phases 3–5) and to the east of the Philippines (phases 5–7) suggests that the MJO index is capable of resolving some of the intraseasonal variability related to the Indian monsoon (Knutson and Weickmann 1987; Maloney and Hartmann 1998; WH).

Similarly constructed plots of the filtered TTL cirrus index regressed onto the time series of each of the phases of the MJO are shown in Fig. 13. In phase 1, a weak maximum in the TTL cirrus field is observed over the equatorial Indian Ocean. From phase 2 to phase 5, this feature intensifies and propagates eastward across the Maritime Continent into the western Pacific. Some reorganization in the cirrus field takes place between phases 3 and 4 (not shown), which seems to be related to the disruption of the convective anomaly as it crosses the Maritime Continent. The cirrus signal over the Pacific weakens during phases 6 and 7 and is no longer apparent in phase 8. The TTL cirrus fields in Fig. 13 exhibit a higher degree of equatorial symmetry than the precipitation fields in Fig. 12. Above the warm pool region and equatorial Africa and South America, regression coefficients between the TTL cirrus index and MJO phase are larger in magnitude by up to a factor of 2 during the boreal winter months than during the boreal summer months (not shown).

In phases 3–6 of Fig. 13, the convectively induced Kelvin–Rossby wave signature, which was documented in the one-point correlation plots in VWFA, is discernible to some degree, with maxima in the TTL cirrus field extending eastward along the equator from the location of maximum positive regression coefficient and flanking the equator to the west of it. A Gill (1980)-like perturbation in the TTL in conjunction with the MJO has also been identified by Hendon and Salby (1994), who focused on tropospheric mean temperatures and 200-hPa winds, and by Tian et al. (2006), who examined 100-hPa temperatures. The Rossby lobes, which are less conspicuous than the Kelvin feature in most of the phases in Fig. 13, are more prominent in composites of total ozone column (Tian et al. 2007).

Comparing Figs. 12 and 13, it can be seen that the TTL cirrus signature is centered between 20° and 30° of longitude to the east of the primary convective center during phases 1–6 (e.g., during phase 2 the precipitation maximum is centered on 85°E, while the TTL cirrus signal is strongest near 110°E). A similar zonal displacement was observed by Eguchi and Shiotani (2004),

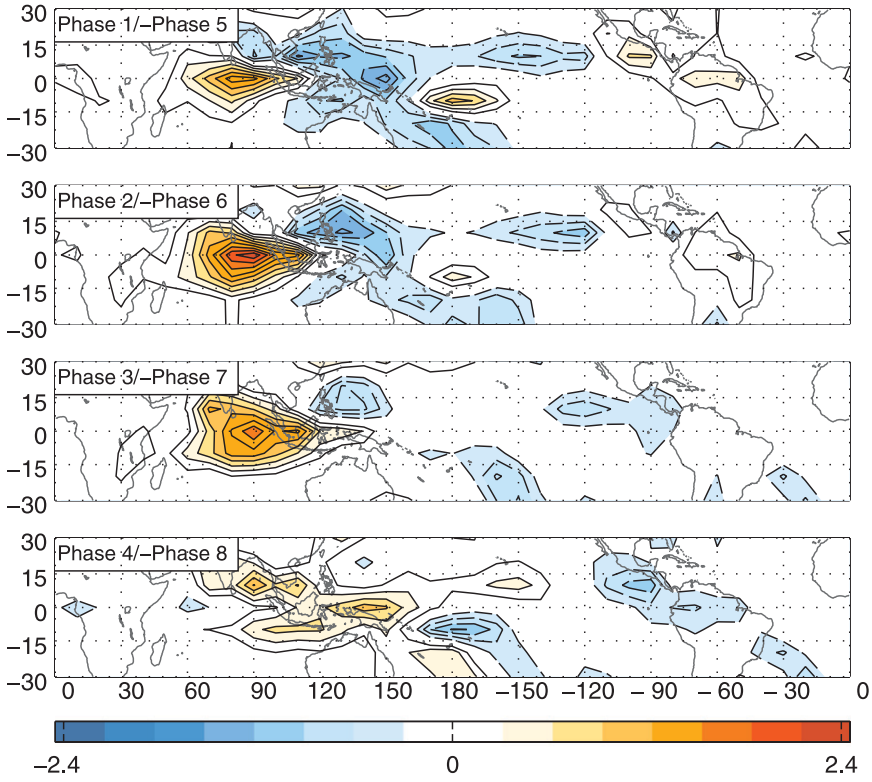

FIG. 12. Filtered 5° latitude × 5° longitude GPCP precipitation (mm day^{-1}) throughout tropics regressed onto phases of MJO index. CI = 0.25.

who created composites of temperature and cirrus occurrence relative to the passage of five different MJO-related convective systems. They observed the lowest 100-hPa temperatures and the highest cirrus cloud fractions at that level between 15° and 25° to the east of the convective centers, implying an eastward tilt with height of the TTL disturbance. Consistent with this interpretation, Schwartz et al. (2008) found positive water vapor anomalies at the 100-hPa level to the east of the enhanced MJO-related convection. A similar displacement is evident in Figs. 6c and 6e in VWFA, which indicate that convection above the Maritime Continent is most strongly correlated with TTL cirrus ~30° of longitude to the east.

Another interesting feature of Fig. 13 is the existence of TTL cirrus maxima over both equatorial South America and Africa during the later stages of the MJO cycle. The cirrus signal over South America during phases 5 and 6 and over Africa during phases 6 and 7 is nearly as strong as the signal over the warm pool region during phases 3–6. The cirrus features over Africa and South America are more narrowly confined to the equatorial belt. These results are in agreement with previous studies of Knutson and Weickmann (1987), Hendon and Salby (1994), and Bantzer and Wallace (1996), which indicate that the upper-level perturbation associated with the MJO circumnavigates the equatorial belt.

Maps of filtered ERA-Interim 100-hPa temperature, vertical velocity, and relative humidity regressed onto phase 2 of the MJO are shown in Fig. 14. The MJO signal in 100-hPa vertical velocity is relatively weak, with an isolated region of ascent centered above the Maritime Continent, centered just to the east of the corresponding enhanced cirrus signature in phase 2 in Fig. 13. Both the 100-hPa temperature and relative humidity fields exhibit a more expansive MJO signal, including Gill (1980)-like features above the Maritime Continent and western Pacific. The Rossby waves centered near 20° latitude above the western Pacific/Australia and near the Americas are particularly well defined in the temperature and relative humidity regressions.

The vertical structure of the cloud field associated with the MJO can be seen more clearly in Fig. 15, in which the filtered equatorial height-dependent cloud index is regressed onto the time series for the respective MJO phases. In phase 1, a cirrus signal is evident between 60° and 110°E, and a weak convective signal in the lower troposphere is visible beneath it, centered slightly to the west of the cirrus signal. Both cloud features intensify and propagate eastward, and, as noted above, the

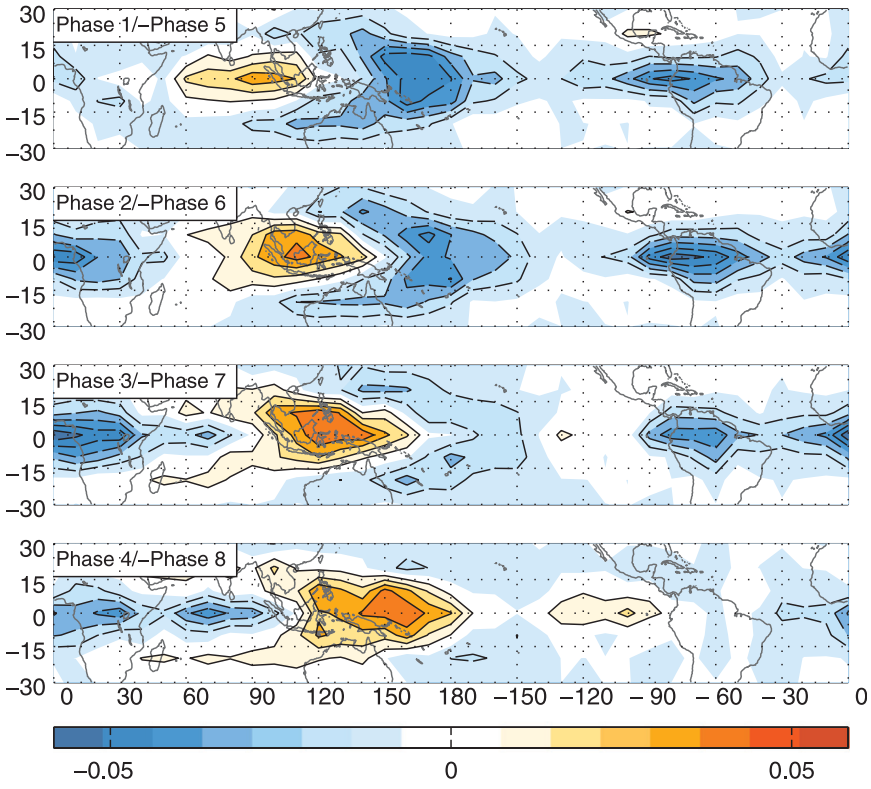

FIG. 13. Filtered CALIPSO TTL cirrus index throughout tropics regressed onto phases of MJO index. CI = 0.01.

convective signature weakens as it crosses the Maritime Continent while the associated cirrus signature undergoes some reorganization. The convective signal becomes less prominent after phase 6 as the convective center shifts off the equator and decays (see Fig. 12). As noted previously, the cirrus feature in phase 1 is centered slightly to the east of the convection. As the MJO evolves, the cirrus feature propagates eastward more rapidly than the convection, eventually leading it by ~30° of longitude. This observation is in agreement with previous work, which has suggested eastward propagation speeds of 3–6 m s^{-1} for MJO-related convection and 10 m s^{-1} for the large-scale circulation features within which the TTL cirrus are embedded (Knutson and Weickmann 1987). An eastward tilt with height is also evident in the cirrus signatures, particularly in phases 1–3; a similar eastward tilt with height was found in equatorial cross sections of Microwave Limb Sounder (MLS)-acquired TTL water vapor anomalies composited relative to the progression of the MJO (Schwartz et al. 2008). As noted in VWFA, this eastward tilt with height is characteristic of the structure of an equatorial Kelvin wave in a stably stratified atmosphere (Holton and Lindzen 1968; Wallace and Kousky 1968; Holton 1979; Roundy 2008).

A cirrus signal above South America (phases 5–7) and Africa (phases 6–8) is also apparent in the vertical regression cross sections in Fig. 15. This feature is smaller in both horizontal and vertical extent than the cirrus signal above the warm pool and displays no noticeable tilt with height. It is also higher in altitude, confined almost completely above the 15-km level, in contrast to the cirrus signature over the Maritime Continent, which extends as low as 12–13 km. From an inspection of the cloud patterns for phases 8 and 1, it is evident that the TTL cirrus maximum is already in place above Africa and the equatorial Indian Ocean as the convective anomaly begins to develop. Whether the circulation feature associated with the TTL cirrus plays a role in initiating the convection of the subsequent MJO episode cannot be determined from this analysis.

The extent to which unfiltered cloud fraction varies during an MJO evolution can be determined from a compositing analysis based on the phase diagram in Fig. 11. Each day of the observation period (June 2006–June 2009) is assigned to whichever of the eight phase vectors that it projects onto most strongly. For this analysis, only days when the magnitude of the MJO vector is greater than one standard deviation from zero are included, so that the 150 days on which the MJO

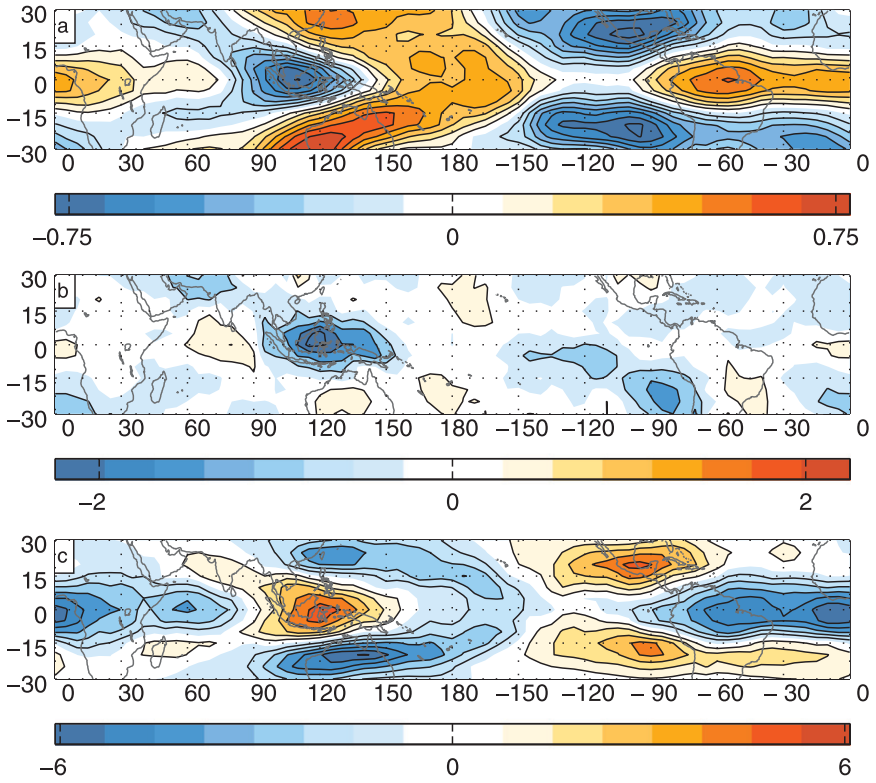

FIG. 14. Filtered 5° latitude × 5° longitude ERA (a) 100-hPa temperature (CI = 0.1°C), (b) 100-hPa ω (CI = 5×10^{-4} Pa s^{-1}; color scale units are 10^{-3} Pa s^{-1}), and (c) 100-hPa relative humidity (CI = 1) regressed onto the MJO phase 2 time series.

signal was weakest, which amount to 13.7% of the total data period, are discarded.

Composite unfiltered TTL cloud fractions and ERA 100-hPa temperatures and winds during two contrasting phases of the MJO (phases 2 and 6) are shown in Fig. 16 [composite plots for all eight phases can be found in Virts (2009)]. Phase 2 corresponds to the early, intensifying stage of the MJO, when the convective maximum is centered near 85°E (see Fig. 12). In phase 2, a TTL cirrus signature is evident in Fig. 16 above the eastern Indian Ocean and Maritime Continent; composite cloud fractions in this region range from 0.15 to 0.2. A region of anomalously low temperatures is collocated with the cirrus feature, with minima in the range of −81° to −80°C. The temperature signature is Gill (1980)-like in shape. Easterly winds prevail within and to the west of the region of maximum cloudiness, particularly above the equator and in the northern subtropics. A region of weak westerly winds is evident to the east of the date line. The Kelvin–Rossby planetary wave signature is much more prominent in the temperature and wind fields in phase 6 and is centered just to the west of the date line; the Rossby lobes in particular are well defined and extend westward over 60° of longitude from the location of minimum temperature. Composite cloud fractions in excess of 0.25 extend over a region stretching from ~155°E to ~170°W, and composite temperatures in this region are as low as ~−83.5°C. The contrast between phases 2 and 6 is even more striking over equatorial South America and Africa. Composite temperatures above these regions are 3°–4°C lower during phase 6, and composite cloud fractions increase from ~0.05 to 0.1 during phase 2 to over 0.3 along the equator during phase 6. Above the warm pool region, composite cloud fractions range from ~0.1 to 0.15 during phases 8 and 1 to ~0.3 in phases 3–5 (not shown).

b. *Variations in tropical-mean TTL cirrus*

The notion that the fields of certain variables averaged over the tropics as a whole pulsate in association with the MJO cycle has been suggested in previous studies (e.g., Hendon 1995). Considering tropical fields that included the zonal mean, Bantzer and Wallace (1996) observed an upper tropospheric temperature signal propagating rapidly (at ~40 m s^{-1}) eastward from the convective region of the MJO following the

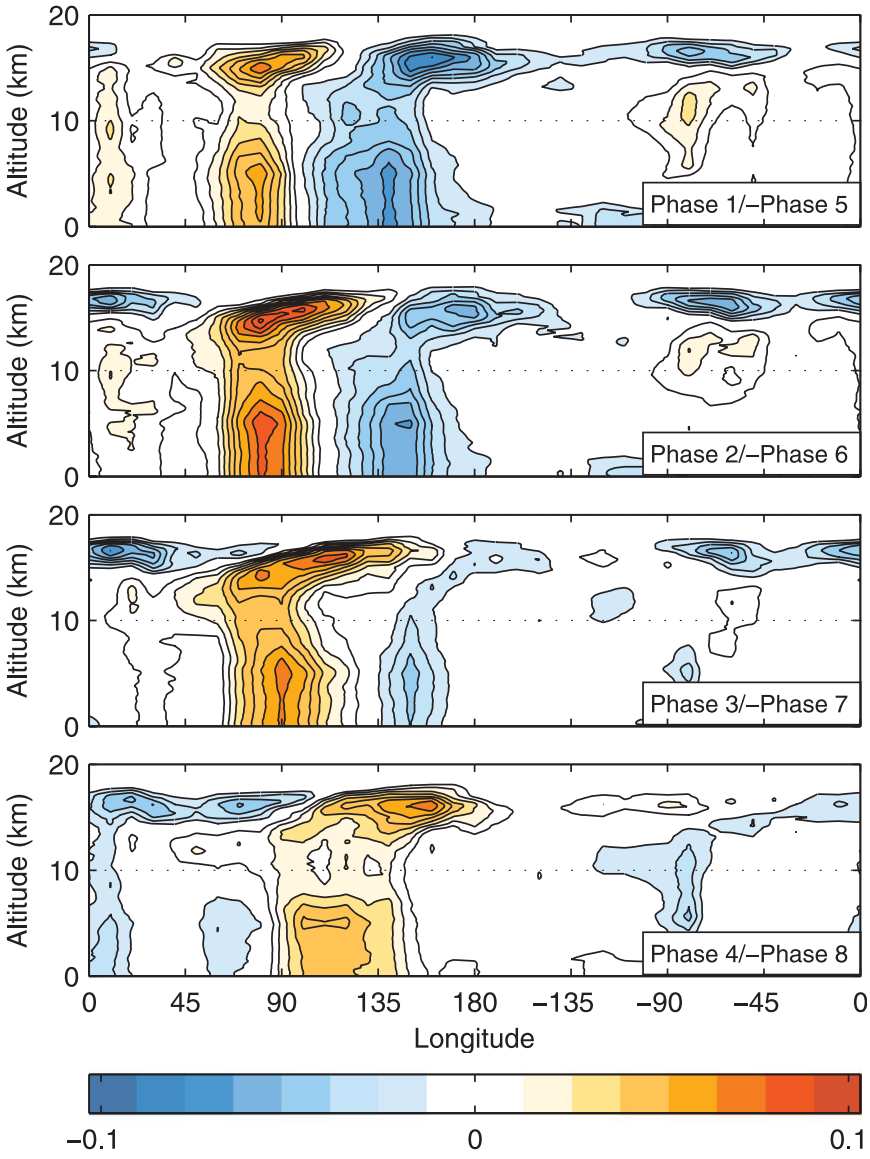

FIG. 15. Longitude–height plots of filtered CALIPSO height-dependent cloud index from 5°S to 5°N regressed onto phases of the MJO index. Longitudinal resolution is 10° (CI = 0.01).

time of maximum tropical-mean precipitation, resulting in a ~0.15°C increase in the tropical-mean upper tropospheric temperature during the MJO's later stages. That the MJO modulates tropical-mean 100-hPa temperature and TTL cirrus is apparent from a close examination of Fig. 16, and this observation is confirmed by the time series of filtered tropical-mean TTL cirrus and 100-hPa temperature, which are plotted in Figs. 17c,d along with the MJO phase 6 time series in Fig. 17e. The unfiltered tropical-mean time series from Fig. 5 are repeated in Figs. 17a,b; for reference, the dates corresponding to the 10 highest peaks in the filtered tropical-mean cloud fraction time series are marked with vertical dashed lines, demonstrating that the MJO signal is discernible even in the unfiltered time series. Colder, cloudier conditions occur during phases 5–7, when MJO-related convective activity is observed above the western Pacific and equatorial Africa and South America (Figs. 12 and 16; Virts 2009). Equatorward of 10° latitude, the mean temperature ranges from −78.6°C in phase 2 to −81.0°C in phase 6, and tropical-mean TTL cirrus fraction ranges over more than a factor of 2, from 0.097 to 0.212; these two phases correspond to the extrema in tropical-mean temperature and cloud fraction (Virts 2009). The correlation coefficient between MJO phase 6 and filtered tropical-mean TTL cirrus fraction

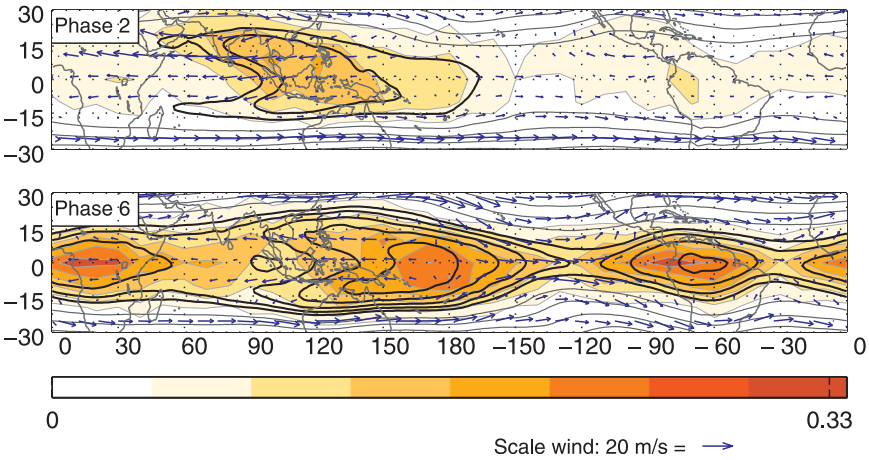

FIG. 16. Composites of unfiltered CALIPSO TTL cirrus index (colors) and ERA 100-hPa temperatures (contours) and winds (vectors) during MJO phases (top) 2 and (bottom) 6, limited to days with magnitude of MJO vector greater than one standard deviation from zero. Cloud fraction CI = 0.05. Temperature contours at . . . −80, −79, −76, −73, . . . °C; outermost dark contour is −79°C.

(100-hPa temperature) is 0.48 (−0.39). These correlations are of similar magnitude to the strongest correlations observed between MJO phase and local TTL cirrus index time series (not shown).

6. Summary and conclusions

In this study, data from the CALIPSO satellite have been used to investigate the impact of the annual cycle, the ENSO cycle, and the Madden–Julian oscillation on TTL cirrus. Based on the results presented above, we can draw the following conclusions:

- The observations of cirrus reveal that the TTL is marked not only by a transition in thermodynamic structure but also by a transition in the structure and evolution of the dominant modes of space/time variability. In the 12–15-km layer, the spatial signatures in the cirrus mirror the patterns in deep convective clouds, which are dominated by the seasonally varying Hadley cell and monsoons and the year-round oceanic convergence zones. The annual cycle at these levels exhibits a high degree of equatorial asymmetry in response to the solar forcing (Fig. 6). The nonseasonal variability on both interannual and intraseasonal time scales exhibits a relatively high degree of spatial complexity and involves pulsations in the strength of semipermanent features (Figs. 9 and 13). As one ascends through the TTL, these characteristic tropospheric signatures become progressively attenuated, and the variability in the cirrus begins to reflect the character of the stratospheric circulation: cloud fraction tends to be higher throughout the tropics during the boreal winter (Figs. 4–6), and the nonseasonal variability exhibits the signature of equatorially trapped Kelvin waves (Figs. 13 and 15). The Kelvin waves associated

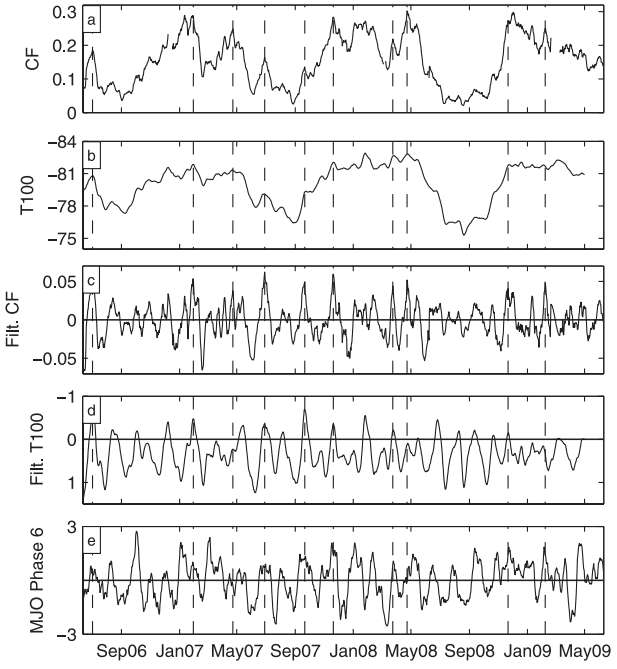

FIG. 17. (a) Seven-day running mean tropical-mean TTL cirrus fraction (cloud fraction with base above 15 km; equatorward of 10°). (b) As in (a), but for ERA 100-hPa temperature (scale is inverted). (c) As in (a), but time series filtered using 80-day high-pass Lanczos filter. (d) As in (c), but time series filtered using 80-day high-pass Lanczos filter. (e) MJO phase 6. Vertical reference lines mark 10 highest peaks in filtered cloud fraction.

with the MJO circumnavigate the globe from west to east with a period of ~40 days, which closely matches the period of the MJO itself. The ENSO cycle is also associated with TTL cirrus signatures that resemble equatorially trapped Kelvin waves (Figs. 9 and 10).

- The maps of filtered cloud occurrence regressed onto MJO phase (Fig. 13) indicate that, while the distribution of TTL cirrus at levels above 15 km is dominated by Kelvin-like, and to a lesser extent Rossby-like, planetary wave perturbations, there is also a land–ocean signature—for example, the passage of planetary waves associated with the MJO is marked by enhanced cirrus over South America and Africa, but not over the contiguous ocean sectors. The land–ocean contrast is also clearly evident in the MJO-related relative humidity field in Fig. 14 but not so much in the temperature field. In general, the MJO signal in the cirrus tends to be concentrated in the regions of high climatological-mean cirrus (Fig. 2a). It is plausible that the ascent and temperature perturbations induced by the passage of the MJO might not be strong enough to induce cirrus formation outside the regions of climatological-mean low temperature and high relative humidity, which lie over the continents. This speculation is supported by comparing Fig. 16 with the left panel of Fig. 12 in VWFA. For example, the latter plot indicates that mean TTL cirrus fractions between 0.2 and 0.3 are observed when temperatures are in the range of −82° to −83°C, which corresponds very well with the observed values above equatorial Africa and South America in the bottom panel of Fig. 16. Temperatures above the equatorial Atlantic and eastern Pacific are relatively higher, near −80° to −81°C, and cloud fractions in those regions are between 0.1 and 0.15, which is also in agreement with Fig. 12 in VWFA.
- Off-equatorial Rossby waves are also more prevalent in the temperature and relative humidity fields in Fig. 14 than in the TTL cirrus field in Fig. 13. The decrease with latitude of 100-hPa relative humidity poleward of ~10° latitude (Fig. 2) offers a possible explanation of our observation that the Rossby wave signatures in the TTL cirrus field are less pronounced than the Kelvin wave signatures. The MJO-related Rossby waves are observed in regions of low background relative humidity. For example, during MJO phases 2–6, twin Rossby features are centered near 20° latitude near the Americas, where annual mean 100-hPa relative humidity is ~40% (Figs. 2 and 14). As demonstrated in Fig. 13 of VWFA, local relative humidities in the range of 50%–70% are required for TTL cirrus occurrence (relative humidities near saturation within the cirrus layer itself are required if the cloud is to persist). Based on these observations, we conclude that TTL cirrus formation within ascending layers in planetary-scale waves is limited to regions in which the ambient relative humidity is sufficiently high, and this constraint results in stronger equatorial Kelvin-like signatures and relatively weaker off-equatorial Rossby wave signatures in the TTL cirrus field.

Both this paper and VWFA have investigated the factors and phenomena that control the location and frequency of occurrence of TTL cirrus layers. We have shown that many of the features in the TTL cirrus field can be interpreted as a remote response to convective heating in the layer below. In this work, we have not considered whether the radiative heating induced by the cirrus layers induces a dynamical response of its own or whether the cirrus should be viewed mainly as a passive tracer. The findings of other ongoing research (e.g., Durran et al. 2009; Dinh et al. 2010) indicate that the heating is capable of inducing a local dynamical response with a vertical wavelength comparable to the cloud layers. It remains to be seen whether this rather localized heating contributes significantly to the generation of vertically propagating planetary waves.

Acknowledgments. The authors thank Todd Mitchell for providing the CTI data and Andrew Gettelman and three anonymous reviewers for their helpful suggestions. This work was supported by the National Science Foundation under Grant 0812802.

REFERENCES

Bantzer, C. H., and J. M. Wallace, 1996: Intraseasonal variability in tropical mean temperature and precipitation and their relation to the tropical 40–50-day oscillation. *J. Atmos. Sci.,* **53,** 3032–3045.

Deser, C., and J. M. Wallace, 1990: Large-scale atmospheric circulation features of warm and cold episodes in the tropical Pacific. *J. Climate,* **3,** 1254–1281.

Dima, I. M., and J. M. Wallace, 2007: Structure of the annual-mean equatorial planetary waves in the ERA-40 reanalyses. *J. Atmos. Sci.,* **64,** 2862–2880.

Dinh, T. P., D. R. Durran, and T. P. Ackerman, 2010: Maintenance of tropical tropopause layer cirrus. *J. Geophys. Res.,* **115,** D02104, doi:10.1029/2009JD012735.

Durran, D. R., T. Dinh, M. Ammerman, and T. Ackerman, 2009: The mesoscale dynamics of thin tropical tropopause cirrus. *J. Atmos. Sci.,* **66,** 2859–2873.

Eguchi, N., and M. Shiotani, 2004: Intraseasonal variations of water vapor and cirrus clouds in the tropical upper troposphere. *J. Geophys. Res.,* **109,** D12106, doi:10.1029/2003JD004314.

Gettelman, A., W. J. Randel, S. Massie, F. Wu, W. G. Read, and J. M. Russell III, 2001: El Niño as a natural experiment for studying the tropical tropopause region. *J. Climate,* **14,** 3375–3392.

Gill, A. E., 1980: Some simple solutions for heat-induced tropical circulation. *Quart. J. Roy. Meteor. Soc.,* **106,** 447–462.

Hendon, H. H., 1995: Length of day changes associated with the Madden–Julian oscillation. *J. Atmos. Sci.,* **52,** 2373–2383.

——, and M. L. Salby, 1994: The life cycle of the Madden–Julian oscillation. *J. Atmos. Sci.,* **51,** 2225–2237.

Highwood, E. J., and B. J. Hoskins, 1998: The tropical tropopause. *Quart. J. Roy. Meteor. Soc.,* **124,** 1579–1604.

Holton, J. R., 1979: *An Introduction to Dynamic Meteorology*. Academic Press, 391 pp.

——, and R. S. Lindzen, 1968: A note on ''Kelvin'' waves in the atmosphere. *Mon. Wea. Rev.,* **96,** 385–386.

Horel, J. D., and J. M. Wallace, 1981: Planetary-scale atmospheric phenomena associated with the Southern Oscillation. *Mon. Wea. Rev.,* **109,** 813–829.

Hsu, H.-H., and M.-Y. Lee, 2005: Topographic effects on the eastward propagation and initiation of the Madden–Julian oscillation. *J. Climate,* **18,** 795–809.

Knutson, T. R., and K. M. Weickmann, 1987: 30–60-day atmospheric oscillations: Composite life cycles of convection and circulation anomalies. *Mon. Wea. Rev.,* **115,** 1407–1436.

Madden, R. A., and P. R. Julian, 1971: Detection of a 40–50 day oscillation in the zonal wind in the tropical Pacific. *J. Atmos. Sci.,* **28,** 702–708.

——, and ——, 1972: Description of global-scale circulation cells in the tropics with a 40–50 day period. *J. Atmos. Sci.,* **29,** 1109–1123.

——, and ——, 1994: Observations of the 40–50-day tropical oscillation—A review. *Mon. Wea. Rev.,* **122,** 814–837.

Maloney, E. D., and D. L. Hartmann, 1998: Frictional moisture convergence in a composite life cycle of the Madden–Julian oscillation. *J. Climate,* **11,** 2387–2403.

Massie, S., A. Gettelman, W. Randel, and D. Baumgardner, 2002: Distribution of tropical cirrus in relation to convection. *J. Geophys. Res.,* **107,** 4591, doi:10.1029/2001JD001293.

Mather, J. H., 2005: Seasonal variability in clouds and radiation at the Manus ARM site. *J. Climate,* **18,** 2417–2428.

McFarquhar, G. M., A. J. Heymsfield, J. Spinhirne, and B. Hart, 2000: Thin and subvisual tropopause tropical cirrus: Observations and radiative impacts. *J. Atmos. Sci.,* **57,** 1841–1853.

Reed, R. J., and C. L. Vlcek, 1969: The annual temperature variation in the lower tropical stratosphere. *J. Atmos. Sci.,* **26,** 163–167.

Ropelewski, C. F., and M. S. Halpert, 1987: Global and regional scale precipitation patterns associated with the El Niño–Southern Oscillation. *Mon. Wea. Rev.,* **115,** 1606–1626.

Roundy, P. E., 2008: Analysis of convectively coupled Kelvin waves in the Indian Ocean MJO. *J. Atmos. Sci.,* **65,** 1342–1359.

Schwartz, M. J., D. E. Waliser, B. Tian, D. L. Wu, J. H. Jiang, and W. G. Read, 2008: Characterization of MJO-related upper tropospheric hydrological processes using MLS. *Geophys. Res. Lett.,* **35,** L08812, doi:10.1029/2008GL033675.

Tian, B., D. E. Waliser, E. J. Fetzer, B. H. Lambrigtsen, Y. L. Yung, and B. Wang, 2006: Vertical moist thermodynamic structure and spatial–temporal evolution of the MJO in AIRS observations. *J. Atmos. Sci.,* **63,** 2462–2485.

——, Y. L. Yung, D. E. Waliser, T. Tyranowski, L. Kuai, E. J. Fetzer, and F. W. Irion, 2007: Intraseasonal variations of the tropical total ozone and their connection to the Madden-Julian oscillation. *Geophys. Res. Lett.,* **34,** L08704, doi:10.1029/2007GL029451.

Virts, K. S., 2009: Cirrus in the tropical tropopause transition layer: Formation mechanisms and influence of local and planetary-scale environment. M.S. thesis, Department of Atmospheric Sciences, University of Washington, 99 pp.

——, J. M. Wallace, Q. Fu, and T. P. Ackerman, 2010: Tropical tropopause transition layer cirrus as represented by CALIPSO lidar observations. *J. Atmos. Sci.,* **67,** 3113–3129.

Wallace, J. M., and V. E. Kousky, 1968: Observational evidence of Kelvin waves in the tropical stratosphere. *J. Atmos. Sci.,* **25,** 900–907.

Wang, P.-H., P. Minnis, M. P. McCormick, G. S. Kent, and K. M. Skeens, 1996: A 6-year climatology of cloud occurrence frequency from Stratospheric Aerosol and Gas Experiment II observations (1985–1990). *J. Geophys. Res.,* **101,** 29 407–29 429.

Wheeler, M. C., and H. H. Hendon, 2004: An all-season real-time multivariate MJO index: Development of an index for monitoring and prediction. *Mon. Wea. Rev.,* **132,** 1917–1932.

Yulaeva, E., and J. M. Wallace, 1994: The signature of ENSO in global temperature and precipitation fields derived from the Microwave Sounding Unit. *J. Climate,* **7,** 1719–1735.

Zhang, C., 1993: On the annual cycle in highest, coldest clouds in the tropics. *J. Climate,* **6,** 1987–1990.

——, 2005: Madden–Julian Oscillation. *Rev. Geophys.,* **43,** RG2003, doi:10.1029/2004RG000158.